CrystEngComm

ROYAL SOCIETY OF CHEMISTRY

PAPER

View Article Online
View Journal | View Issue

Cite this: *CrystEngComm*, 2022, **24**, 7200

In vitro crystallization of calcium carbonate mediated by proteins extracted from *P. placenta* shells†

Ningjing Song, Jiangfeng Li, Baosheng Li, Ercai Pan, Juan Gao and Yurong Ma *

The shells of *P. placenta* are composed of foliated calcite laths packed as layered structures and have high mechanical properties and optical transparency. However, the biomineralization mechanism and the influence of the organic matrix on the formation of the foliated calcite laths in the shells of *P. placenta* are not known. The acid-soluble matrix (ASM) was extracted from the shells of *P. placenta* and characterized in detail. Sixteen proteins including calcium-binding and chitin-binding proteins were associated to shell formation *via* proteome analysis of ASM. The ASM was found to be enriched with Gly, Asp and Ser. By tracking the Ca^{2+} concentration in the solution in the presence of ASM by a potentiometric method, we find that the ASM has a strong effect to stabilize the amorphous calcium carbonate (ACC) precursor in solution with a nucleation time of about 7733 s and a retardation factor of about 2.3, while the concentration of the ASM was 0.3 μg mL^{-1}. In particular, the ASM can inhibit the (secondary) nucleation of calcium carbonate for 10 and 24 hours on the shell surfaces of *P. placenta* and the glass substrate in the aqueous solution, respectively. An explosive secondary nucleation and quick crystal growth from 50 nm to 10 μm can be finished on the shell surfaces in one hour, in between 10 h and 11 h of reaction time, *via* a gas diffusion process. This indicates that the ASM has a very strong effect to stabilize ACC and inhibit nucleation. The formation of ACC in the solution and its transformation to calcite crystals on the substrates were tracked by dynamic light scattering, selected-area electron diffraction, infrared spectroscopy, scanning electron microscopy, and confocal laser scanning microscopy. It was found that the ASM was doped in the preliminary nanocrystals with a size of about 50–100 nm, which were formed on the shell surfaces *via* secondary nucleation, and was occluded into the calcite crystals without preferred adsorption on particular crystal planes. The calcite crystals formed on the shell surfaces became more and more rounded and lost {104} planes with increasing concentration of the ASM in the solution, indicating that the ASM can stabilize other planes instead of the thermodynamic {104} planes. The *in vitro* crystallization study in this work shows that ASM extracted from the shells of *P. placenta* has a strong effect on the biomineralization process of foliated calcite laths of *P. placenta*.

Received 20th May 2022,
Accepted 26th September 2022

DOI: 10.1039/d2ce00692h

rsc.li/crystengcomm

1 Introduction

Calcium carbonate is one of the most popular biominerals in marine animals such as mollusks, corals and echinoderms,[1–3] and calcium carbonate has been an important model system to study the biomineralization and bioinspired mineralization processes for decades.[4–11] Calcium carbonate has polymorphs such as calcite, vaterite, aragonite, monohydrate calcite, ikaite ($CaCO_3 \cdot 6H_2O$), and calcium carbonate hemidydrate.[10,12] Biogenic calcite minerals exist in the prism layers of mollusk shells, tests and spines of echinoderms and foliated crystals in bivalves.[13–15] Foliated calcite is a very interesting kind of morphology of biogenic calcite minerals, which are packed as layers in the shells. *P. placenta*, also known as windowpane oyster, has shells composed of foliated calcite single crystals with a thickness of about 300 nm, packed as layered structures. The *c* axis of the calcific laths is tilted about 24.4° ± 3.5° from the normal direction of the shell surface, and the surfaces of the laths are close to the {108} planes of calcite according to the literature.[16,17] The shells of *P. placenta* are very thin and possess a unique optical property of ~80% total transmission of visible light.[18] The hardness of the shell of *P. placenta* increases ~55% in comparison to that of single-crystal calcite.[18,19] Recently, our research group annotated the

School of Chemistry and Chemical Engineering, Beijing Institute of Technology, Beijing 100081, China. E-mail: yurong.ma@bit.edu.cn

† Electronic supplementary information (ESI) available. See DOI: https://doi.org/10.1039/d2ce00692h

unigenes of the mantle tissue of *P. placenta* by using public databases such as nr, GO, KOG, KEGG, and Pfam.[20] We proposed that four unigenes with the highest expression levels in the mantle tissue are very often related to the biomineralization process, while another three unigenes are potentially related to the biomineralization process according to quantitative real-time polymerase chain reaction (qRT-PCR) analysis.

Amorphous calcium carbonate (ACC) is an important intermediate precursor of the formation process of biogenic calcium carbonate minerals[21,22] in the *in vitro* crystallization process.[23–26] The formation pathways, stability and crystallization of ACC particles under different synthesis conditions were investigated.[27–29] *In situ* transmission electron microscopy (TEM) and cryo-TEM studies have been employed to investigate the nucleation and growth of $CaCO_3$.[9,30–32] Using cryo-TEM and computer simulation, the possible structural forms of pre-nucleation clusters (PNCs) are proposed to be chain-, ring-, and branch-like and isolated nanometer-sized structures.[33,34] The existence of PNCs was initially evidenced during the early stages of ACC formation by potentiometric titration and analytical ultracentrifugation.[8,35,36] To investigate the roles of additives in ACC, some remarkable studies have been presented. For example, Polystyrene sulphonate (PSS) increases local supersaturation, resulting in ACC nucleation only at the sites of the globules.[37] Mg^{2+} can regulate the phase transformation pathway from ACC to calcite in a concentration-dependent manner.[38,39] The capping of triethylamine (TEA) is used to stabilize the precursors, which is defined as $(CaCO_3)_n$ ionic oligomers. If the density of oligomers is increased, the crosslinking of ionic oligomers leads to the rapid construction of a pure monolithic ACC.[11] In addition, the stability of ACC particles is also influenced by the amount of water contained in them.[40–42]

Biological molecules play important roles in Ca^{2+} transportation, stabilization of ACC, inhibition of nucleation and the biomineralization process of calcium carbonate in organisms.[43,44] Kong *et al.* identified that PNU9 extracted from *Pinctada fucata* was able to inhibit the crystal growth of $CaCO_3$ and inhibit ACC transformation to calcite.[45] As a typical acidic protein, Asprich mollusk shell protein can transiently stabilize ACC and tune $CaCO_3$ crystallization.[46] Recombinant Pif from the nacreous layer of *P. fucata*,[47] acidic abalone nacre protein perlwapin[48] and EDTA-soluble matrix protein PfY2 from both the prismatic layer and the nacreous layer of *P. fucata*[49] clearly inhibited the transformation of ACC to calcite or aragonite in the *in vitro* system.[47,49] Matrix protein Alv extracted from the prismatic layer could promote nucleation and stimulate calcite crystallization while inhibiting transition from ACC to aragonite.[50] Lys (K)-rich mantle proteins (KRMPs), prismalin-14 and aspein extracted from prismatic layers play a critical role in calcite formation.[51–53] The addition of ovalbumin, AP8 and starmaker-like proteins to the reaction changed the morphology of crystals from rhombohedral to 'stack-like' structures.[54–56] Furthermore, mixed proteins were extracted from molluscan shells by EDTA, weak acid and water, and the influence of these proteins on the *in vitro* crystallization of calcium carbonate was investigated. EDTA-soluble protein from abalone nacre can induce the nucleation and growth of calcite seed crystals.[57] EDTA-soluble ubiquitylated proteins in the prismatic layer of *P. fucata* can reduce the rate of calcium carbonate precipitation and induce calcite formation.[58] Furthermore, the water-soluble matrix and acid-soluble matrix extracted from abalone and pearl shells can strongly influence the final polymorph and morphology of $CaCO_3$.[59–61] Moreover, the ASM was identified from nacre and prismatic layers by proteomics in the pearl oyster *Pinctada margaritifera* and *Pinctada maxima*,[62] greenlip abalone *Haliotis laevigata*,[63] and abalone *Haliotis asinine*.[64] However, little is known about the influence of the ASM of the shells with foliated calcite crystals on the biomineralization process and the *in vitro* crystallization of $CaCO_3$, as far as we know.

In this study, the ASM was extracted from the shells of *P. placenta* and characterized by proteome analysis. The influence of the ASM on the *in vitro* crystallization process of calcium carbonate was investigated by a gas diffusion method. Potentiometric titrations reveal that the ASM has a strong effect to stabilize the ACC precursor in the solution. *In vitro* crystallization of the calcite system shows that the ASM can inhibit the (secondary) nucleation of calcium carbonate for 10 and 24 h on the shell surfaces of *P. placenta* and the glass substrate in the aqueous solution. Our results show that the ASM is occluded in the crystals and influence the crystallization process.

2 Materials and methods

2.1 Materials

Sodium hypochlorite solution was bought from Macklin (Shanghai, China). Acetic acid–sodium acetate buffer was bought from Yuanye (Shanghai, China). The Amicon ultracentrifugal filter unit was bought from Merck Millipore (Darmstadt, Germany). The BCA assay kit was bought from TransGen Biotech (Beijing, China). The HiTrap™ desalting column (5 mL) was bought from GE company (Boston, USA). Coomassie brilliant blue was bought from Rhawn (Shanghai, China). Calcium chloride ($CaCl_2$), sodium carbonate (Na_2CO_3), ammonium carbonate [$(NH_4)_2CO_3$], trometamol, sodium bicarbonate ($NaHCO_3$), sodium hydroxide (NaOH), hydrochloric acid (HCl) and sulfuric acid (H_2SO_4) were bought from Aladdin (Beijing, China). Iodoacetamide, ammonium bicarbonate (NH_4HCO_3), amino acid standard solution and proteomics grade trypsin (from bovine pancreas) were from Sigma (Darmstadt, Germany). HPLC grade acetonitrile (CH_3CN), trifluoroacetic acid (TFA), formic acid (FA), ethanol and dithiothreitol (DTT) were all bought from Merck (Darmstadt, Germany). Sulfo-cyanine 5 NHS ester (Cy5) was bought from Bioorth (Nanjing, China). Sodium dodecyl sulfate (SDS), 40% acrylamide/methyl bisacrylamide (ratio 37.5 : 1) and 10% ammonium persulfate were bought

from Sinopharm (Shanghai, China). Prestained broad-range protein molecular weight marker was bought from Vazyme company (Nanjing, China).

2.2 Shell matrix protein extraction

Shells were collected from fresh 2-year-old adult *P. placenta* (6–10 cm in length) during July to August (2020) from Beibu Gulf (Fangchenggang City, Guangxi Province, China). The shells were washed with 3% sodium hypochlorite to remove contaminants on the surfaces. The shells were then washed with water for 5 min and dried in air. A grinder was used to grind the shell pieces into powder, which was then graded using a 200 μm mesh. The powder (5 g) was then decalcified with 150 mL acetic acid–sodium acetate buffer (pH 3.8) for 5 h at 4 °C under continuous agitation. For extraction of the ASM, the supernatant was collected by centrifugation at 4000 rpm for 30 min at 4 °C and was then concentrated using an Amicon ultrafiltration system on a Millipore membrane dialysis filter (YM10; 10 kDa cutoff). The concentrated solution (about 1 mL) was extensively desalted using a 5 mL desalting column (HiTrap™ GE, USA) against Milli-Q water. The concentration of the protein was measured using a BCA assay kit (TransGen Biotech) according to the manufacturer's instructions. Sodium dodecyl sulfate-polyacrylamide gel electrophoresis (SDS-PAGE) analysis of the purified protein was performed as reported in the literature.[65]

2.3 Proteomics analysis

The ASM was stained with Coomassie brilliant blue and the entire protein lane was separated into four pieces (Fig. 1b, P1–P4), which were completely destained by washing with 50 μL of a 50 mM NH_4HCO_3/CH_3CN (50/50) mixture for 30 min at 37 °C. Then, the destained solution was removed from the 1.5 mL microcentrifuge tube with the ASM. 50 μL of reducing buffer containing 10 mM DTT and 50 mM NH_4HCO_3 was added to the 1.5 mL tube with the ASM for 1 h at 57 °C. Alkylation was performed with 50 μL of 100 mM iodoacetamide for 30 min at RT in the dark. The gel pieces were dried in CH_3CN and treated with 0.4 μg trypsin in 10 μL of 50 mM NH_4HCO_3 for 12 h at 37 °C with shaking. The solution was placed in a clean tube and treated with 50 μL of 1% formic acid at 30 °C for 30 min under agitation. The digestion solution was then lyophilized and suspended in 30 μL of 0.1% trifluoroacetic acid and 4% acetonitrile for LC-MS/MS analysis. 5 μL of sample was injected into a Q Exactive HF-X mass spectrometer with a Thermo EASY-nLC system for analysis. MS data were acquired automatically using Analyst QS 1.1 software (Applied Biosystems), following a MS survey scan over *m*/*z* 350–1500 at a resolution of 60 000 for full scan and 2000 for MS/MS measurements.

The LC-MS/MS data were compared with the protein database downloaded from the molluscan category in the NCBI database using a Mascot 2.1 search engine with carbamido-ethylated cysteine as a fixed modification and oxidized methionine and tryptophan as variable modifications. No other post-translation modification has been performed. Notably, a newly assembled *Crassostrea gigas* genome uploaded by the Chinese Academy of Sciences was available, which highly increased the number of identified proteins. The peptide MS and MS/MS tolerances were set to 0.5 Da. Finally, sequences with mascot scores of at least 5.0 and with at least two matched peptide fragments were considered as valid data.

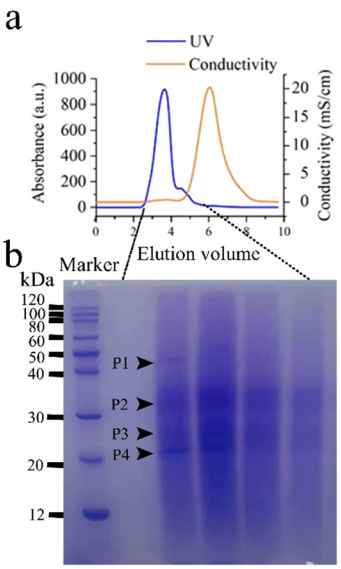

c

Amino acid	Percentage (mol %)*
Asp	13.57
Thr	0.89
Ser	13.32
Glu	3.82
Gly	17.65
Ala	2.37
Cys	0
Val	1.12
Met	0.31
Ile	0.35
Leu	1.36
Tyr	2.84
Phe	1.22
Lys	1.09
His	0.67
Arg	3.23
Pro	0.63

Fig. 1 Global compositions of the ASM of *P. placenta* shell. (a) Desalting the ASM solution using a HiTrap™ desalting column; the UV plot represents the absorbance intensity at 280 nm, which indicates the intensity of the ASM of the elution. (b) SDS-PAGE fractionation of foliated layer ASM; the ASM reveals various distinct proteinaceous bands (P1–4) that were further investigated by proteomics. (c) Amino acid compositions of the ASM from the *P. placenta* shell. *Values are expressed by the quotient of the amount of amino acid and that of the reference of the standard amino acid mixture.

2.4 Amino acid composition

In preparation for amino acid analysis, the ASM was hydrolyzed under vacuum in 6 M HCl at 110 °C for 24 h. Samples and amino acid standards (Sigma) were analyzed on a Hitachi L8900 automated amino acid analyzer and quantified by ninhydrin reaction.

2.5 Potentiometric titrations

The pre- and post-nucleation stages of $CaCO_3$ were investigated by titration assays, in which both the Ca^{2+} potential and the pH of the solutions were collected with time. For this purpose, a fully automated commercial system provided by Metrohm (Filderstadt, Germany) was used. The setup consisted of a Titrando 907 titration device with two Dosino 800 dosing units. A polymer-based ion-selective electrode (ISE, Metrohm no. 6.0510.110) and a flat-membrane glass electrode (Metrohm no. 6.0262.100) were used to monitor the free Ca^{2+} concentration and pH, respectively.

Carbonate buffers with a pH of 9.00 were prepared by mixing 10 mM solutions of sodium carbonate and sodium bicarbonate in appropriate ratios. The protein solutions were extensively desalted using a 5 mL desalting column (HiTrap™ GE, USA) against Milli-Q water. Eventually, the protein concentration was adjusted to 0.01 mg mL^{-1}. For measurement, 25 mL of carbonate buffer (with or without protein) was filled into a beaker, and 0.01 M $CaCl_2$ solution was titrated at a rate of 0.01 mL min^{-1} while automated counter-titration of 0.01 M NaOH was applied to keep the pH of the buffer constant at 9.00 ± 0.05. Calibration of the Ca^{2+} ISE was achieved by titration of 0.01 M $CaCl_2$ into water under the same conditions. In general, ISE calibration is performed by correlating measured calcium potentials, $U(Ca^{2+})$, with known analytical Ca^{2+} concentrations, $c(Ca^{2+})$, using a Nernstian approach.[8] It can be described as

$$U(Ca^{2+}) = U_0 + \frac{RT}{2F}\ln[c(Ca^{2+})] \quad (1)$$

where $U(Ca^{2+})$ is the measured potential, U_0 is the electrode intercept, R is the gas constant, T is the temperature, and F is the Faraday constant. Eqn (1) is transformed into:

$$\ln[c(Ca^{2+})] = a + b\cdot U(Ca^{2+}) \quad (2)$$

The values of the intercept a and the slope b of eqn (2) were obtained from the linear fit of the calibration data. All solutions were prepared with water of Milli-Q quality. During titrations, the beakers were continuously flushed with a gentle stream of nitrogen to avoid CO_2 uptake from the atmosphere.

2.6 *In vitro* crystallization experiments in aqueous solution with ASM

$CaCl_2$ solutions of 5 mM were prepared and then preserved in a refrigerator at 4 °C. The aqueous solutions containing the ASM were prepared with a concentration of 2 mg mL^{-1} and then frozen at −80 °C. Calcium carbonate crystals were precipitated in the desiccator by a gas diffusion method.[66] For a standard *in vitro* precipitation experiment, a glass beaker containing 10 g $(NH_4)_2CO_3$ and two small glass beakers containing 1 mM H_2SO_4 solution were kept inside a desiccator, and 5 mM of $CaCl_2$ solution with 10 μg mL^{-1} ASM was kept in a bottle; small pieces of the inner shell surface of *P. placenta* or glass were put at the bottom of the bottle, which was covered with Parafilm punched with needle holes and then put in a desiccator. After a certain reaction time, the precipitates in the solution or on the surfaces of shells or glass were collected, washed, and dried at room temperature for later characterization.

2.7 Preparation of Cy5-labelled proteins

Proteins (1 mL, 2 mg mL^{-1}) were mixed with 100 μL Cy5 (dissolved in Milli-Q water, 1 mg mL^{-1}) and then the solution was incubated for 30 min. The labeled ASM was desalted into DDW using a HiTrap™ desalting 5 mL column in an AKTA™ protein purification system (GE, USA). The entire process was conducted in the dark. The final proteins are designated as Cy5-ASM.

2.8 Characterization

The precipitates collected from the solutions or on the substrates at the bottom of the reaction solution after a certain time were characterized by using polarized light microscopy (OLYMPUS, BX53, Japan), field-emission scanning electron microscopy (SEM, JEOL JSM-7500F, Japan) at an accelerating voltage of 15 kV, transmission electron microscopy (TEM, JEOL 2010F at 200 keV), and confocal laser scanning microscopy (CLSM, Nikon N-SIM, Japan) at 645 nm. Dynamic light scattering (DLS, Zetasizer Nano ZS-90) was applied to characterize the solutions at the very early stage of the *in vitro* reaction systems.

3 Results

Analysis of the ASM of the shells

An efficient on-line desalting process using molecular weight cut-off centrifugal filtration was applied to analyze the global compositions of the ASM of *P. placenta* shells in this study. An on-line desalting AKTA™ protein purification system was employed for simultaneous desalting and detection of the ASM. Fig. 1a indicates that the ASM and salt were efficiently separated on the HiTrap™ desalting column. The ASM were harvested and condensed by ultrafiltration and SDS-PAGE. The ASM extracted from foliated calcite shells of *P. placenta* were stained with Coomassie brilliant blue and exhibited a few distinct proteinaceous bands *via* SDS-PAGE (Fig. 1b). SDS-PAGE indicated proteins with abundant bands at 40–50 kDa, 30–40 kDa, and 20–30 kDa, as well as the presence of a blue smear throughout the entire lane, which indicate that part of the ASM proteins were degraded in SDS-PAGE.

The ASM was enriched with amino acids such as Gly, Asp and Ser (Fig. 1c). These proteinaceous bands were further investigated by LC-MS/MS for protein identification. A set of sixteen proteins were identified from the ASM of the foliated calcite of *P. placenta* shells according to the LC-MS/MS analysis and *C. gigas* genome indexed in the UniProt database (Table 1). The identified proteins were roughly divided into five categories based on the protein domain analysis and their putative functions: (1) calcium-binding proteins: EF-hand calcium-binding domain-containing protein 6 (EFCB6), hemicentin-1 and epidermal growth factor-like domains protein 6 (EGFL6); (2) framework-associated proteins: chitin-binding type 4 domain-containing protein (ChBD4), chitin synthase, collagen-like, collagen alpha-1(IV) (COL4-α1) and von Willebrand factor A (VWA); (3) potential mineralized protein: elongation factor 1-alpha (EF1-α); (4) immune-related proteins: C1q domain-containing protein (C1qDC); (5) other proteins: heat shock 70 kDa protein (HSP70), WD repeat-containing protein 34 (WDR34),

Table 1 Proteome analysis for the ASM from the shell of *P. placenta*[a]

Accession	Description	Protein domain	MW (kDa)	Function	Ref.
K1R9E2	EF-hand calcium-binding domain-containing protein 6 (EFCB6)	EF-hand	20.7	Ca^{2+}-binding	67
K1QTK8	Multiple epidermal growth factor-like domains protein 6 (EGFL6)	EGF-like	14.5	Cell adhesion, signaling, and Ca^{2+}-binding	68
K1R2P7	Hemicentin-1	Immunoglobulin-like (Ig-like)	43.5	Ca^{2+}-binding	69
K1QGM1	Chitin synthase	Myosin motor	27.1	Involved in metabolism of chitin	70
K1QE07	Chitin-binding type- 4 domain-containing protein (fragment) (ChBD4)	Chitin-binding type- 4	24.7	Binding chitin scaffolds	71
K1Q335	Collagen-like protein 7	Collagen	23.8	Structure protein for the nucleation of calcium carbonate	72, 73
K1RH30	Collagen alpha-1(IV) (COL4-α1)		160.8		
K1P6L3	Von Willebrand factor A and EGF domain-containing protein (VWA and EGF)	VWA, EGF	80.6	Binding collagen, binding chitin; crystal morphology	68, 74
K1REU8	Von Willebrand factor A and EGF domain-containing protein (VWA and EGF)		25.3		
K1QGS8	Elongation factor 1-alpha (EF1-α)	EF1_GN	50.4	Involved in biomineralization	75
K1PDE0	C1q domain-containing protein (C1qDC)	Complement 1q (C1q)	31.9	Immune-related molecules	76
K1QWR0	Heat shock 70 kDa protein (HSP70)	HSP70	67.6	Assist in the folding of nascent proteins	77
K1P6U6	F-box/WD repeat-containing protein 7 (FBXW7)	Trp-Asp repeat (WD repeat)	91.9	Serve as scaffolds in assembling functional complexes	78
K1R5F1	WD repeat-containing protein 34 (WDR34)		56.1		
K1RPB4	WD repeat-containing protein 91 (WDR91)		75.4		
K1RE93	WD repeat-containing protein 87 (WDR87)		21.9		

[a] The first column is the accession number of the protein, which could be indexed in the UniProt database.

WD repeat-containing protein 91 (WDR91), WD repeat-containing protein 87 (WDR87).

Titration analysis

The influence of the ASM on the stability of amorphous calcium carbonate (ACC) was investigated by using titration analysis. 0.01 mol L^{-1} $CaCl_2$ solution was added to Na_2CO_3 buffer solution at a constant rate of 0.01 mL min^{-1}, while the pH of the buffer was kept constant at 9.00 by automated counter titration of NaOH aqueous solution. The potentials of the $CaCl_2$ solution with known concentrations were collected and math fitting was done by using eqn (2). On that basis, the free Ca^{2+} concentrations in the carbonate buffer were obtained from the measured potentials and eqn (2) by dosing $CaCl_2$ solutions with unknown concentrations into the carbonate buffer. The dashed black line in Fig. 2a represents the concentration of Ca^{2+} added to the carbonate buffer at pH 9.0. The free Ca^{2+} concentration shown in the *Y*-axis was tracked and calculated according to the potentials measured by an ion-selective electrode *via* eqn (2), while the *X*-axis shows the Ca^{2+} concentration added to the solution, $[c_{add}(Ca^{2+})]$, which increases at a constant rate with time.

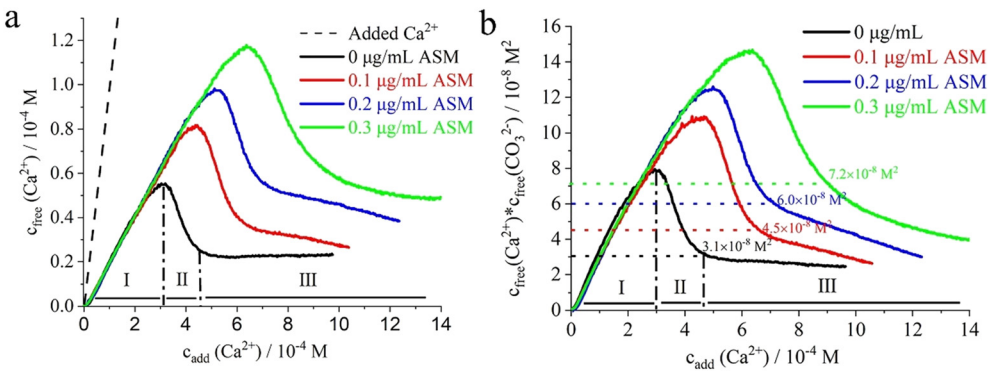

Fig. 2 Potentiometric titration assays in the presence of the ASM with different concentrations. (a) Development of the free Ca^{2+} concentration as a function of the added Ca^{2+} concentration. The dashed black line represents the concentration with Ca^{2+} during titration. (b) Corresponding free ion solubility products, calculated under the assumption that Ca^{2+} and CO_3^{2-} bind in equimolar ratios in both the pre- and the post-nucleation stages. Dotted lines of different colors indicate the solubility of the initially precipitated phase in the presence and absence of the ASM. I depicts the prenucleation stage, II the nucleation stage, and III shows the $CaCO_3$ particle growth stage.

Linear increase of the free Ca^{2+} concentrations, $[c_{free}(Ca^{2+})]$, can be observed while the added Ca^{2+} concentrations $[c_{add}(Ca^{2+})]$ were low (Fig. 2a, stage I). It can be seen that the free Ca^{2+} concentrations increased linearly and reached a maximum while $[c_{add}(Ca^{2+})]$ increased to some certain values. It is supposed that no precipitate or prenucleation of $CaCO_3$ formed in the solution before $[c_{add}(Ca^{2+})]$ reached a maximum. The $[c_{free}(Ca^{2+})]$ decreased with a sharp slope until it reached a plateau region, which indicates that the free Ca^{2+} concentrations were quickly consumed by precipitation, and quick crystal nucleation formed at this $[c_{add}(Ca^{2+})]$ window (stage II). Nucleation occurs when a critical point is reached and the amount of free calcium drops to a value that corresponds to the solubility of the precipitated phase.

The maximum $[c_{free}(Ca^{2+})]$ in the solutions increased from 0.82×10^{-4} M to 1.17×10^{-4} M, while the ASM concentrations added to the carbonate solution increased from 0.1 μg mL^{-1} to 0.3 μg mL^{-1}. The higher the ASM concentrations, the higher the maximum $[c_{free}(Ca^{2+})]$ in the solution. It is known that biological calcium carbonate mineralization utilizes a nonclassical nucleation scheme that involves the initial formation of nanometer-sized prenucleation clusters (PNCs) that assemble into larger clusters of amorphous calcium carbonate (ACC).[8,27,79–81] The post-nucleation solubility product decreases relative to the reference state yet still indicates the formation of an ACC mineral phase.[80,81] In the prenucleation stage (stage I), the binding of Ca^{2+} in ion pairs and/or large ion clusters is evident from the difference of added and free Ca^{2+} concentrations, as described in detail elsewhere.[8] At some critical point, the nucleation of a second phase (ACC) takes place and the $[c_{free}(Ca^{2+})]$ decreases quickly and eventually levels off at a plateau (stage II). The slope of the free Ca^{2+} development in the prenucleation stage thereby reflects the thermodynamic equilibrium constant of PNC formation.[82] In comparison to the control curve for the solution without the ASM, the slopes for the free Ca^{2+} concentrations do not change significantly with the increase of the concentrations of the ASM (Fig. 2a), which suggests that the ASM does not interfere with the formation equilibria of PNCs at all tested concentrations.

The $[c_{add}(Ca^{2+})]$ shown on the *x*-axis for the titration assays plots can be changed with time since the Ca^{2+} was added at a constant rate to the solutions (Fig. S1†). Corresponding nucleation times for the samples increased from 3417 s to 7733 s while the ASM concentrations increased from 0.1 μg mL^{-1} to 0.3 μg mL^{-1}, which indicate that the ASM has the ability to stabilize the prenucleation clusters or the intermediate amorphous precursor $CaCO_3$ in the solution[80,81,83] (Table 2). This time interval difference can be quantitated by a retardation factor (*F*), which is the quotient of the average nucleation time in the presence of the ASM and the solution without the ASM (Table 2). The retardation factor increased dramatically from 1.5 to 2.3 with increasing ASM concentrations.

Furthermore, titration experiments allow for a quantitative determination of the solubility of the precipitated particles. For the corresponding solubility product constant (K_{sp}) of $CaCO_3$, the product of free calcium and carbonate ions $[c_{free}(Ca^{2+})\cdot c_{free}(CO_3^{2-})]$ is written as follows:[27]

$$c_{free}\left(Ca^{2+}\right)\cdot c_{free}\left(CO_3^{2-}\right) = c_{free}\left(Ca^{2+}\right)\cdot\frac{\Lambda\left(CO_{3,aq.}^{2-}\right)_{pH}\left[n_{total}(\text{carbonate}, t=0) - n_{bound}(Ca^{2+}, t)\right]}{V(t)} \quad (3)$$

where $\Lambda(CO_{3,aq.}^{2-})_{pH}$ is the pH-dependent fraction of carbonate, $n_{bound}(Ca^{2+}, t)$ is the moles of bound calcium ions. $\Lambda(CO_{3,aq.}^{2-})_{pH}$ in eqn (3) is calculated according to eqn (4):

$$\Lambda\left(CO_{3,aq.}^{2-}\right)_{pH} = \left[\frac{c(H^+)^2}{K_1K_2} + \frac{c(H^+)}{K_2} + 1\right]^{-1} \quad (4)$$

The acid constants are given by $pK_1 = 6.35$ and $pK_2 = 10.33$. K_1 and K_2 are the first and second dissociation constants of the carbonate buffer. The concentration of hydrogen ions is given by $pH = -\log[c(H^+)]$. Thus, after nucleation, the solubility product constant (K_{sp}) of $CaCO_3$ can be obtained by using the above equations and the concentrations obtained *via* titration tests. Fig. 2b shows the variation of the concentration products of free calcium and carbonate ions ($c_{free}(Ca^{2+})\cdot c_{free}(CO_3^{2-})$) with the increase of the $[c_{add}(Ca^{2+})]$ and the protein concentrations, while the junction points of the second stage (the nucleation stage) and the third stage (the growth stage) indicate the K_{sp} of $CaCO_3$ of the systems. The concentration products shown in the *Y*-axis were obtained from measuring free concentrations of Ca^{2+} with the ion-selective electrode and calculating the CO_3^{2-} concentrations *via* eqn (3), while the *X*-axis shows the increase of the Ca^{2+} concentration added to the solution. The K_{sp} of $CaCO_3$ in the solution without protein was 3.1×10^{-8} M^2, which is consistent with the reported solubility of ACC with a calcite short-range order in the literature.[8] The K_{sp} of $CaCO_3$ in the solution in the presence of 0.1 μg mL^{-1} ASM was 4.5×10^{-8} M^2. The K_{sp} of $CaCO_3$ was increased from 6.0×10^{-8} M^2 to 7.2×10^{-8}

Table 2 Calcium potentiometric titration data obtained for the ASM and reference (protein deficient) samples

Concentration of ASM	Nucleation time (s)	Retardation factor *F*	Prenucleation slope (M s^{-1})	K_{sp}/solubility (M^2)
Reference (0 μg mL^{-1})	3417	—	1.66×10^{-10}	3.1×10^{-8}
0.1 μg mL^{-1}	5125	1.5	1.60×10^{-10}	4.5×10^{-8}
0.2 μg mL^{-1}	6115	1.8	1.58×10^{-10}	6.0×10^{-8}
0.3 μg mL^{-1}	7733	2.3	1.51×10^{-10}	7.2×10^{-8}

M^2, while the concentrations of the ASM increased from 0.2 μg mL^{-1} to 0.3 μg mL^{-1} (Table 2). The K_{sp} value of ACC in solution in the presence of Asp at pH 9.00 was about 4–5 × 10^{-8} M^2.[84] The high K_{sp} values of $CaCO_3$ in the solutions with the ASM indicate the formation of the intermediate phase, or amorphous phase. The higher the concentration of the ASM, the higher the K_{sp} values, and the higher the stability of the ACC phase, which is consistent with the literature.[82,85–87] This was consistent with previous reports for small ubiquitin-like modifier, a glycine-rich region with K_{sp} ≈ 5.96 × 10^{-8} M^2 at 1 mg mL^{-1}.[87] Very high K_{sp} values have been reported in the systems with a polymer-induced liquid precursor (PILP) phase by using additives such as sodium triphosphate (K_{sp} ≈ 40 × 10^{-8} M^2 at 0.1 mg mL^{-1}) and poly-(aspartic acid) (K_{sp} ≈ 20 × 10^{-8} M^2 at 0.1 mg mL^{-1}).[82] Finally, our results suggest that the ASM considered here can stabilize ACC phases.

Effect of the ASM on the early stage of the *in vitro* crystallization of $CaCO_3$

Interaction with Ca^{2+} is an important characteristic of calcification-related proteins. Thus, the possible Ca^{2+}-binding ability of the ASM was investigated by simple mixing. The Tyndall effect can be observed from the $CaCl_2$ solution mixed with 10 μg mL^{-1} ASM, while no Tyndall effect existed in the ASM solution or $CaCl_2$ solution (Fig. S2a†). The Tyndall effect in the $CaCl_2$ solution mixed with 10 μg mL^{-1} ASM indicates that aggregates are formed by Ca^{2+} and the ASM in the $CaCl_2$ solution. The aggregates were collected with centrifugation and washed with double-distilled water (DDW) and characterized by using TEM and selected-area electron diffraction (SEAD) (Fig. S2b†). It shows that the aggregates are composed of interconnected sheet-like and fibrous structures with some dark nanoparticles, which are amorphous phase according to SAED. Energy-dispersive spectroscopy (EDS) analysis indicates the presence of C, N, O and Ca in the aggregates (Fig. S2c and d†). Thus, it is proposed that the agglomerates are complexes of protein and Ca^{2+}. The Tyndall effect of the $CaCl_2$ solution with the ASM disappeared when ethylenediaminetetraacetic acid (EDTA) was added to the mixed solution (Fig. S2a†), which indicates that aggregates composed of complexes of protein and Ca^{2+} disappeared since EDTA can decompose proteins.

As for the standard conditions, calcium carbonate crystallization experiments were carried out in an aqueous solution with 5 mM $CaCl_2$ and 10 μg mL^{-1} ASM at room temperature by using a gas diffusion method. Generally, *P. placenta* shells with polished inner surfaces and a size of about 5 mm × 5 mm were put at the bottom of the beakers with the reaction solutions. The precipitates formed in the solutions at the early stage were collected by centrifugation, washed with DDW and characterized by TEM, SAED and SEM. Dark nanoparticles with a size of about 20 nm and a fiber-like structure in gray can be observed after 20 min of reaction from the TEM image, which were in the amorphous phase according to SAED (Fig. 3a). EDS analysis indicates that the atomic ratio of O and Ca is 3 : 1 (Fig. S3†), very close to that in $CaCO_3$, which is much lower than that of O and Ca of the complexes of ASM and Ca^{2+} formed before the addition of ammonium carbonate in Fig. S2† (21 : 1). The fiber-like structures are complexes of ASM and Ca^{2+} ions. The spherical nanoparticles are much darker than the fiber-like structures.

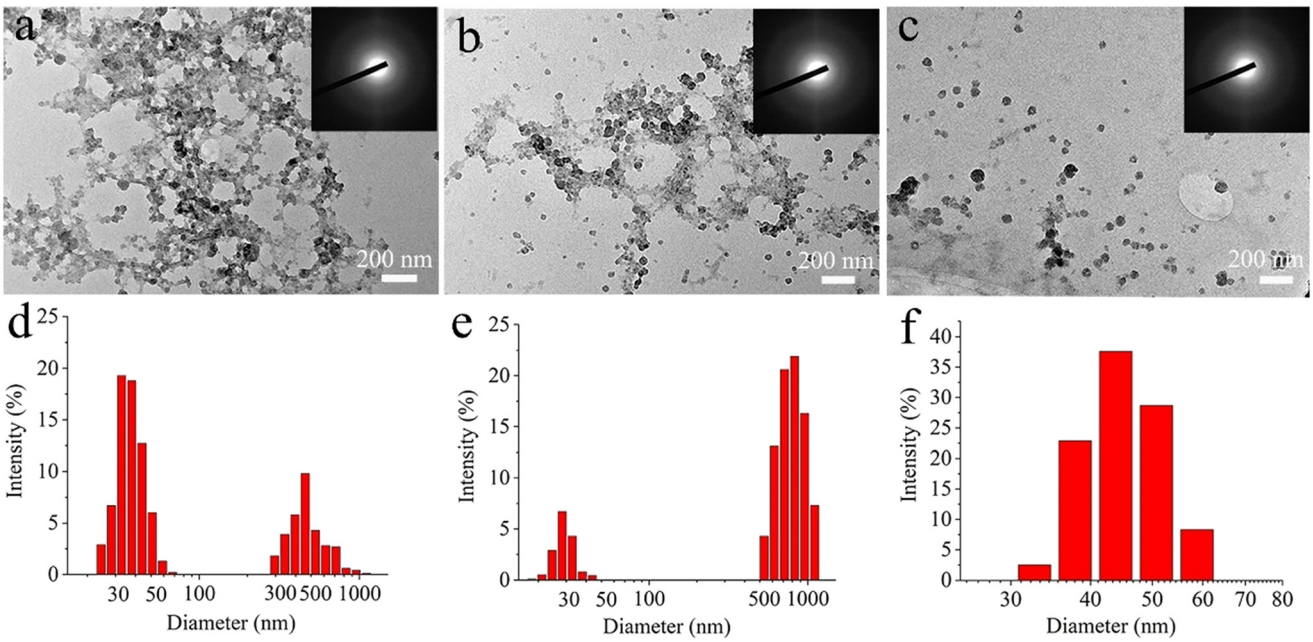

Fig. 3 TEM images and DLS results of the obtained nanoparticles collected from the reaction solutions after certain reaction times under otherwise standard conditions. (a and d) 20 min, (b and e) 40 min, (c and f) 1 h. Inset images in the TEM micrographs are selected-area electron diffraction patterns obtained for the center area of the TEM images, which show an amorphous pattern.

Dynamic light scattering analysis indicates that there are two kinds of particles with sizes of about 20–30 nm and 500–1000 nm (Fig. 3d), supposed to be the spherical nanoparticles and fiber-like structures in Fig. 3a. More nanoparticles and less fiber-like structures formed in the solution while increasing the reaction time to 40 min and 1 h, which are in the amorphous phase according to SAED (Fig. 3b and c). Interestingly, only isolated spherical nanoparticles appeared and the fiber-like agglomerates disappeared after 60 min of mineralization (Fig. 3c). The sizes of the nanoparticles increased from 30–50 nm to 40–60 nm while increasing the reaction times from 40 min to 1 h and only one kind of size can be observed after 1 h (Fig. 3e and f). Based on the above TEM and SEM analyses, we propose that the spherical nanoparticles are amorphous calcium carbonate (ACC), since ammonium carbonate was present and CO_2 would diffuse into the reaction solutions. Fiber-like complexes of ASM and Ca^{2+} ions transferred to ACC in the solution in the presence of CO_2 after 1 h.

The reaction solution was still clear and the Tyndall effect can still be observed in the solution after 2 h of reaction (Fig. 4a, inset). The precipitates collected after 2 h of reaction show uniform spherical nanoparticles with a size of about 50 nm (Fig. 4a). Meanwhile, the nanoparticles after 2 h of reaction were still in the amorphous phase according to the SAED pattern (inset of Fig. 4b). The FTIR spectrum shows the split vibration band at around 1500 cm^{-1} and the band at 865 cm^{-1}, which are assigned to the asymmetric stretching (ν_3) and out-of-plane bending (ν_2) of the carbonate groups of ACC, respectively.[88] The FTIR spectrum shows a direct proof that the nanoparticles formed at the early stage of the reaction (20 min–2 h) are ACC. Polarized light microscopy images indicate that the nanoparticles obtained after 2 h have no birefringence feature but transformed to crystalline particles with an obvious birefringence feature after they were kept in an environment with 100% room humidity (RH) at room temperature for 48 h (Fig. S4†). The transformation from non-birefringence to birefringence under 100% RH is another proof that the nanoparticles are ACC.[2] The nanoparticles from the solution were collected and observed with TEM imaging and diffraction from 4 h to 8 h in the presence of 10 μg mL^{-1} ASM (Fig. S5†). Interestingly, they were apparently amorphous (SAED pattern in Fig. S5†). In addition, almost no nanoparticles were observed on the shell surfaces of *P. placenta* from 0 h to 8 h (Fig. S6†). These results indicate that the ASM can stabilize ACC nanoparticles.

Effect of ASM on the *in vitro* crystallization of $CaCO_3$ on the shell surfaces

To track the formation process of $CaCO_3$ on the shells, the precipitates formed on the shell surfaces of *P. placenta* after different reaction times were characterized by SEM. The shell surfaces are smooth and clean, and no nanoparticles can be observed on the shell surfaces under SEM after 10 h of reaction time (Fig. $5a_1$–a_4), similar to the SEM images of the shell surfaces from 0 to 8 h (Fig. S6†). However, rhombohedral calcite crystals in micrometer size were formed after 30 min on the shell surfaces in solution in the absence of the protein (Fig. S7†).

Nanoparticles with sizes from 20 nm to 40 nm can be clearly seen on the edges of the foliated calcite laths of *P. placenta* and most areas of the surfaces of the calcite laths are free of nanoparticles when the reaction time was 10.17 h (Fig. $5b_1$–b_4). The amounts and sizes of the nanoparticles on the edges increased and the amount of the nanoparticles with big sizes (~50 nm) increased while the reaction time extended to 10.33 h (Fig. $5c_1$–c_4). No specific faces can be seen from the spherical nanoparticles. Obvious rhombohedral morphology can be observed on the shell surfaces when the reaction time was extended to 10.5 h, marked with arrows (Fig. $5d_1$–d_4). We assumed that these nanoparticles with rhombohedral shapes are calcite nanocrystals formed on shell surfaces, and we assume that the spherical nanoparticles observed in Fig. $5b_1$–b_4 and c_1–c_4, formed 10 or 20 min earlier than those in Fig. $5d_1$–d_4, might be crystalline calcite nanoparticles which formed *via* secondary nucleation, which still have no observable rhombohedral shapes at the very early forming stage. We

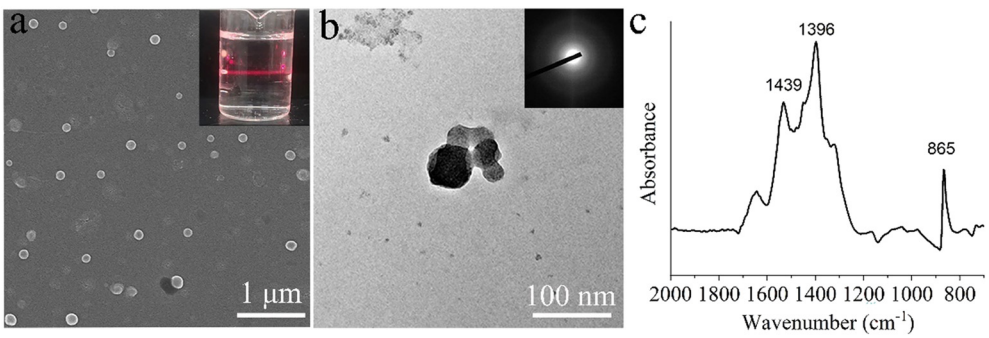

Fig. 4 Characterization of the obtained nanoparticles collected from the reaction solutions after 2 h of reaction time under otherwise standard conditions. (a) SEM image. Inset: the solution exhibited a Tyndall effect, which clearly indicates the presence of significant amounts of nanoparticles in the solution. (b) TEM image. The inset shows the corresponding SAED pattern of the nanoparticles which indicates that they are amorphous. (c) FTIR spectrum.

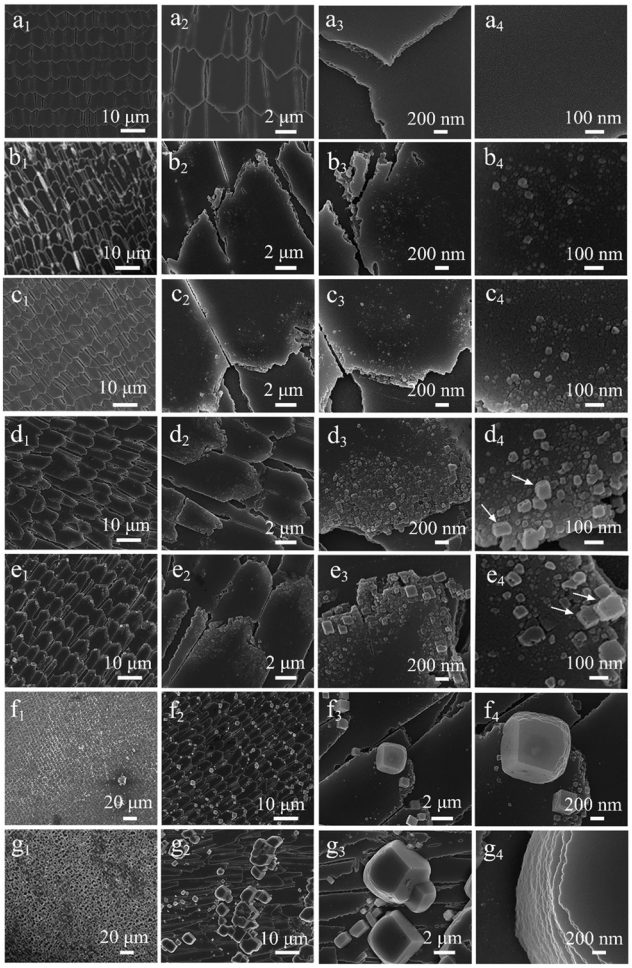

Fig. 5 SEM images of the formation process of $CaCO_3$ on the shell surfaces of *P. placenta* after different reaction times under otherwise standard conditions. (a_1–a_4) 10 h, (b_1–b_4) 10.17 h, (c_1–c_4) 10.33 h, (d_1–d_4) 10.5 h, (e_1–e_4) 10.67 h, (f_1–f_4) 10.83 h and (g_1–g_4) 11 h. White arrows denote the location of representative rhombohedral crystals.

know that ACC nanoparticles with sizes of about 20–50 nm exist in the solution from 2 h to 8 h (Fig. 4 and S5†) and no nanoparticles precipitate on the shell surfaces after 10 h (Fig. 5a_1–a_4). This indicates that the ACC nanoparticles in the solution are very stable for a long time (10 h) and a quick "secondary nucleation" process triggers the crystallization process. The rhombohedral particles are larger than 100 nm when the reaction time was 10.67 h (Fig. 5e_1–e_4). The rhombohedral particles have ordered patterns on the shell surfaces. It can be concluded that these rhombohedral particles are calcite crystals formed *via* secondary nucleation and epitaxial growth which have the same crystal orientation as the foliated calcite laths of *P. placenta*.

A lot of rhombohedral calcite crystals with sizes varying from 200 nm to 2 μm were formed on the short edges of the foliated calcite laths when the reaction time was extended to 10.83 h (Fig. 5f_1–f_4) and the sizes of the rhombohedral calcite crystals increased to about 8 μm (Fig. 5g_1–g_4). A uniform layer of rhombohedral calcite crystals formed on the shell surfaces. Three smooth {104} planes can be seen on the rhombohedral crystals, while the other faces are cambered and rough. Layered structures with cambered steps can be seen on the rhombohedral crystals. We assume that these cambered steps were formed due to the presence of the ASM, similar to the role of organic molecules reported in the literature,[56,89–92] considering that rhombohedral calcite nanocrystals with maximum sizes of about 100 nm were formed on the shell surfaces after 10.5 h when the ASM concentration in the solution was 10 μg mL^{-1}. The ACC nanoparticles were kept in the amorphous phase from 1 h to 8 h according to the TEM images and SAED patterns. However, calcite microcrystals with a size of about 10 μm were formed after 30 min on the shell surfaces in the solution without the ASM. Thus, it is clear that the ASM can strongly inhibit the nucleation of calcite crystals. Once the secondary nucleation started and nanoparticles precipitated on the shell surfaces, after 10.17 h, the crystal growth is a very fast process. It took about 20 min for the nanoparticles to grow from 50 nm (10.5 h) to 2 μm (10.83 h), while it took another 10 min for the crystals to further grow to about 8 μm. We consider that the fast growth process also contributed to the strong stabilization ability of ASM for ACC, and a large amount of ACC was stored in the solution until the secondary nucleation was triggered and the growth became an explosive process.[93]

Fig. 6a shows the SEM image of the pure shell of *P. placenta* with smooth and clean foliated calcite laths before *in vitro* $CaCO_3$ crystallization. The shells of *P. placenta* before and after the *in vitro* crystallization process have strong diffraction peaks of {104} and {10$\underline{1}$0}, indicating the strong crystalline orientation of the shells of *P. placenta* and the rhombohedral calcite microcrystals grown on the shell surfaces (Fig. 6c). Patterns of oriented calcite microcrystals with {104} faces parallel to each other can be observed in the SEM images in Fig. 5g_3 and 6b. The crystal orientation results from PXRD are consistent with the SEM results, which exhibit oriented calcite microcrystals grown on the shell surfaces *via* a secondary nucleation and epitaxial growth process. The calcite crystals grown on the shell surfaces were scraped and characterized with TEM and SAED, which show (104), (110), and (01$\bar{4}$) planes of the single crystalline calcite diffraction pattern (Fig. S8†).

Distribution of ASM in calcite crystals

According to the above results, ASM can stabilize ACC in the solution and inhibit the nucleation of calcite crystals. Also, the *in vitro* synthesized calcite crystals became rounded and part of the {104} faces disappeared. It is proposed that ASM stabilized some particular planes and thus induced the formation of rounded calcite crystals with "imperfect" {104} faces. To understand whether ASM occludes in the calcite crystals or adsorbs on particular crystal planes of calcite during the *in vitro* crystallization process, ASM was labeled with fluorescent dye Cy5-NHS ester (Cy5-ASM) and then applied as an additive to the *in vitro* crystallization process under similar conditions. The

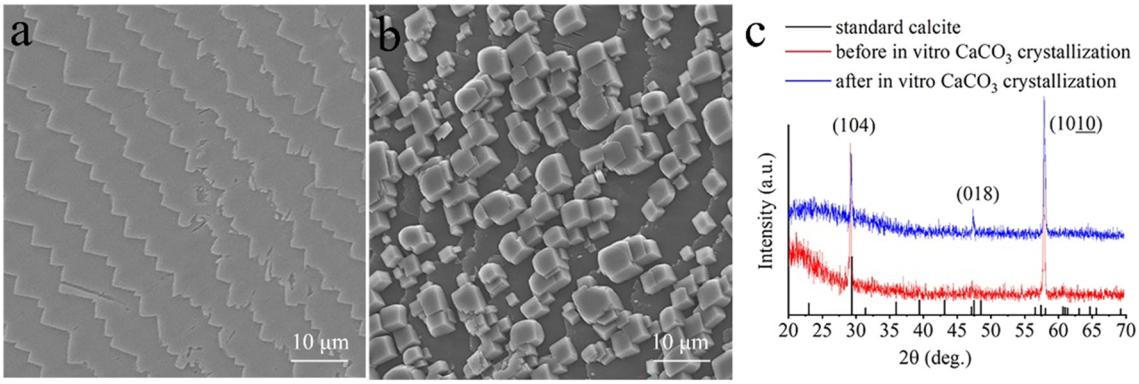

Fig. 6 PXRD characterization of the $CaCO_3$ formed on the shell surfaces of *P. placenta* after 11 h of reaction time under otherwise standard conditions. SEM images of the shell before (a) and after (b) *in vitro* $CaCO_3$ crystallization. (c) PXRD patterns of the shell substrates in (a) and (b).

crystallization time was set as 11 h. To rule out the influence of Cy5 dye on the crystallization, *in vitro* crystallization was also done by using Cy5 as an additive, instead of ASM, under similar conditions. All the samples obtained after 11 h of reaction time were characterized by using confocal laser scanning microscopy (CLSM) at an excitation wavelength of 645 nm (Fig. 7). The bright-field images show the formation of calcite microcrystals on the shell surfaces (Fig. $7a_2$–c_2). No fluorescence signal was observed from the two samples precipitated in the presence of Cy5 dye or unlabeled ASM (Fig. $7a_1$–a_3 and b_1–b_3). In comparison, fluorescence signals can be observed from most of the calcite microcrystals on the shell surface (Fig. $7c_3$). A zoomed-in image of one calcite crystal is shown in the inset of Fig. $7c_3$. To further investigate whether Cy5-ASM was occluded in the calcite crystals, CLSM images with different depths were collected on one calcite crystal and thus the 3D distribution of fluorescence signals can be given by these CLSM images. Two CLSM images show uniform fluorescence signals on the two orthogonal transverse cross sections (Fig. $7c_4$ and c_5), which indicates that Cy5-ASM distribute uniformly in the calcite microcrystals. CLSM images along other cross sections show a similar homogenous fluorescence intensity. These CLSM results clearly imply that the ASM indeed occludes into the calcite crystals without specific adsorption on particular crystal planes.

CLSM characterization was also applied to track the location of ASM in the calcite crystals during the whole *in vitro* crystallization process by using Cy5-ASM as an additive (Fig. 8). CLSM images show that slight fluorescence signals were noticeable on the edges of the foliated calcite laths of the inner shell surface of *P. placenta* after 10.17 h (Fig. $8a_1$–a_3). Considering that the nanoparticles precipitated on the shell surface in the SEM images in Fig. $5b_1$–b_4, it is assumed that ACC nanoparticles precipitated together with ASM on the shell surfaces. The fluorescence signals became stronger and the size with strong fluorescence signals increased while extending the reaction time from 10.17 h to 10.83 h (Fig. $8b_1$–e_1). The fluorescence signals increased with the growth of the calcite crystals on the shell surfaces, clearly indicating that ASM is involved in the whole crystal formation process (Fig. $8b_3$–e_3). Thus, the CLSM images further confirmed that ASM is not just adsorbed on the crystal surfaces but actually occluded inside the crystals.

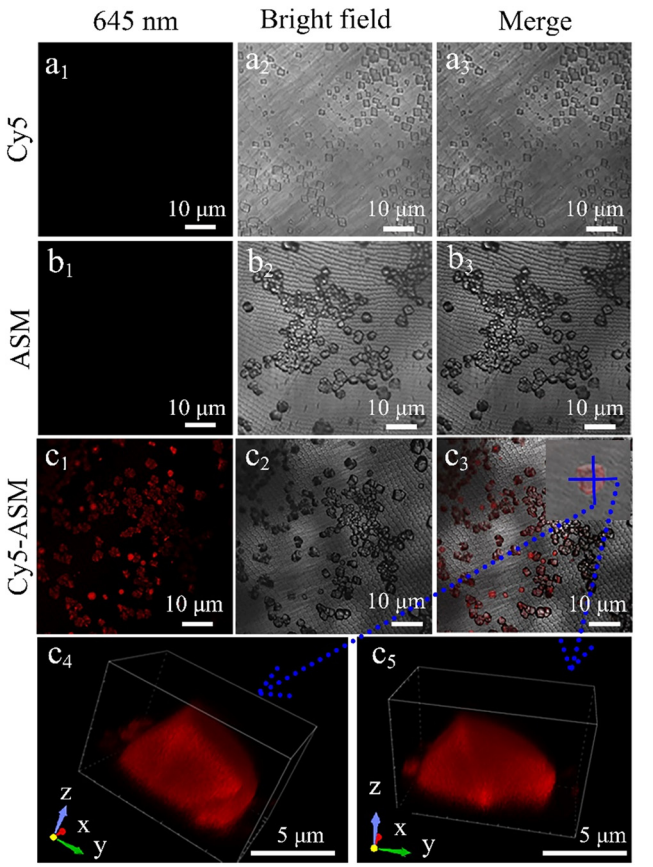

Fig. 7 CLSM of the $CaCO_3$ formed on the shell surface of *P. placenta* in the presence of different additives after 11 h of reaction time under otherwise standard conditions. (a_1–a_3) Cy5, (b_1–b_3) ASM, (c_1–c_3) Cy5-ASM. Inset: the CLSM of one calcite crystal shown in (c_3). (a_1–c_1) Images obtained at 645 nm laser excitation. (a_2–c_2) Images obtained at bright field. (a_3–c_3) Merged images obtained from the CLSM images and bright-field images. (c_4 and c_5) 3D confocal images of the two orthogonal transverse cross sections are obtained from (C_3 inset), as indicated by dotted blue arrows.

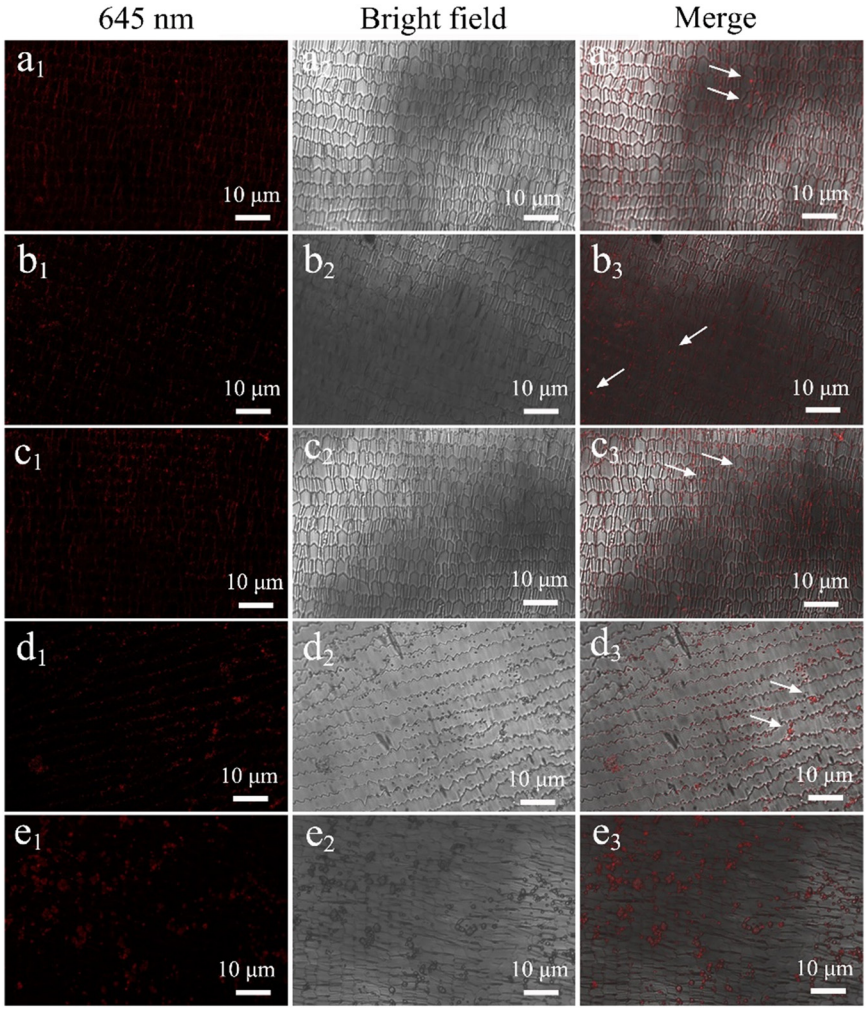

Fig. 8 CLSM of the formation process of $CaCO_3$ on the shell surface of *P. placenta* after different reaction times under otherwise standard conditions. (a_1–a_3) 10.17 h, (b_1–b_3) 10.33 h, (c_1–c_3) 10.5 h, (d_1–d_3) 10.67 h, (e_1–e_3) 10.83 h. (a_1–e_1) Images obtained at 645 nm laser excitation. (a_2–e_2) Images obtained at bright field. (a_3–e_3) Merged images obtained from the CLSM and bright-field images. White arrows denote the location of representative fluorescence signals, respectively.

Functions of different concentrations of ASM

The *in vitro* crystallization process was also allowed to proceed for 12 hours by changing the concentrations of ASM under otherwise standard conditions (Fig. 9). Calcite crystals formed on the shell surfaces in the absence of the protein show perfect rhombohedral morphology with well-developed {104} faces (Fig. $9a_1$–a_3). In comparison, the crystals in the ASM group show significant changes in crystal morphology. Calcite crystals grown in a solution with 5 μg mL^{-1} ASM were also rhombohedral with very minor edge truncations (Fig. $9b_1$–b_3). The calcite crystals formed on the shell surfaces became rounded with increasing concentrations of ASM in the solution (Fig. $9c_1$–c_3 and d_1–d_3), indicating that the ASM can stabilize other planes instead of the thermodynamically stable {104} planes. Fig. 10 shows the Raman spectra of four kinds of calcium carbonate crystals formed on the shell surfaces in the presence of ASM with different concentrations, corresponding to the samples shown in Fig. 9. As shown in Fig. 10, the three vibration bands at 281 cm^{-1}, 712 cm^{-1}, and 1086 cm^{-1} are typical vibration bands of the carbonate of calcite.

Fig. S9† shows the SEM morphologies of $CaCO_3$ formed on glass substrates after different reaction times in the presence of ASM, or after 6 h of reaction time without ASM. It was shown that rhombohedral calcite crystals in micrometer size were formed after 6 h on the glass substrate in solution in the absence of ASM (Fig. S9a†). However, no particles or crystals can be observed on the glass substrate after 18 h of reaction time (Fig. S9b†). Rounded calcite crystals can be observed on glass surfaces after 24 h (Fig. S9c†), which are similar to that obtained on shell surfaces after 11 h of reaction time in Fig. 5. These results indicate that ASM can very strongly inhibit the nucleation of calcium carbonate on glass substrates, and secondary nucleation becomes relatively easier, which starts after 10 h of reaction.

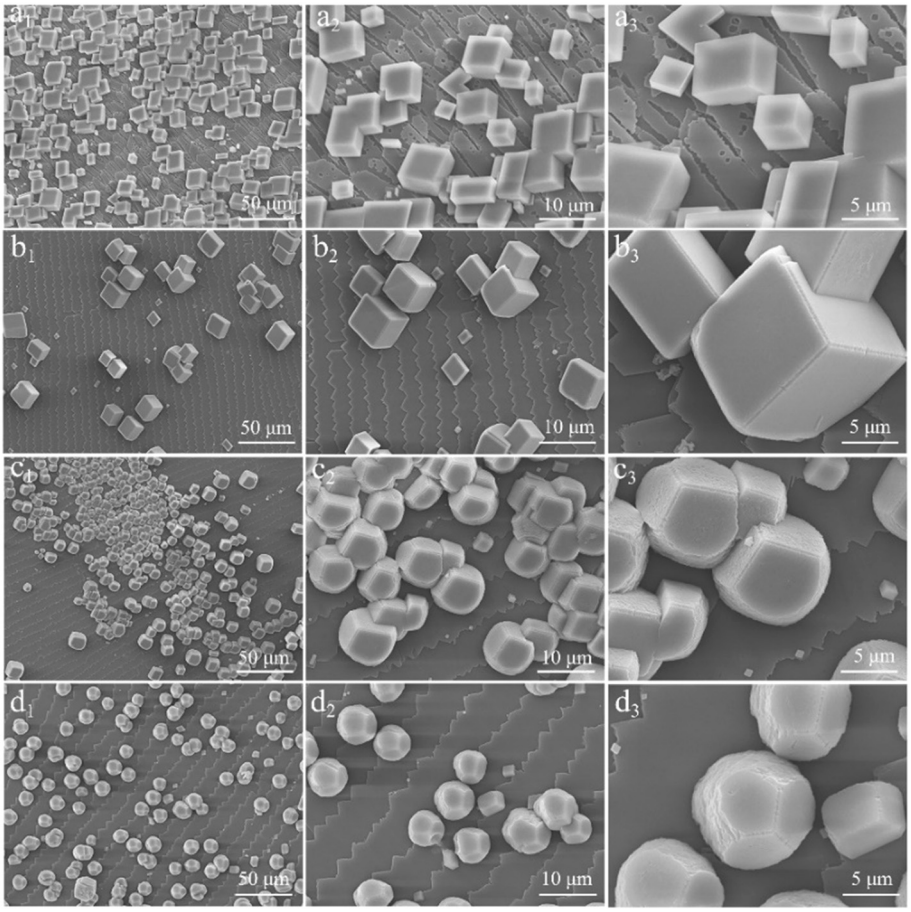

Fig. 9 SEM images of $CaCO_3$ formed on the shell surfaces of *P. placenta* in the presence of ASM with different concentrations after 12 h of reaction time under otherwise standard conditions. (a_1–a_3) 0 μg mL^{-1}, (b_1–b_3) 5 μg mL^{-1}, (c_1–c_3) 10 μg mL^{-1}, (d_1–d_3) 15 μg mL^{-1}.

4 Discussion

We find that ASM extracted from the shells of *P. placenta* has a strong influence on the *in vitro* $CaCO_3$ crystallization process. Proteomics analysis shows that there are four framework-associated proteins, three Ca^{2+}-binding proteins, one potentially mineralization-related protein and a few other proteins in the ASM according to proteomics analysis. The four framework-associated proteins, Ca^{2+}-binding proteins and potentially mineralization-related proteins are all probably related to the biomineralization process of the shells of *P. placenta*. Four framework-associated proteins including chitin synthase, chitin-binding, collagen and VWA domain-containing proteins found in *P. placenta* were also reported to be related to chitin assembly and/or the subsequent biomineralization process.[70–73,94–97] Collagens have been identified from many molluscan shells including *Mytilus*,[94,95] *Hyriopsis cumingii*,[96] and *Pinctada fucata*[97] and were reported to be related to the nucleation of calcium carbonate.[73] The VWA domain is a cell adhesion domain generally found in association with extracellular proteins and has the ability to bind collagen.[69,74]

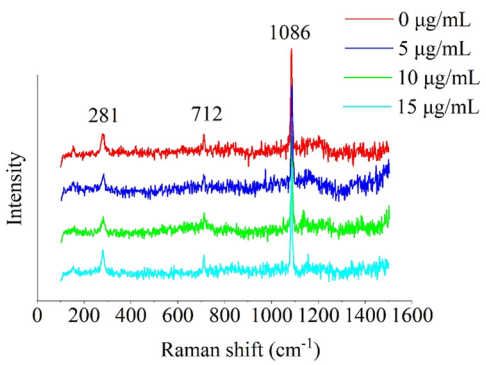

Fig. 10 Raman spectra of $CaCO_3$ formed on the shell surfaces of *P. placenta* in the presence of ASM with different concentrations after 12 h of reaction time under otherwise standard conditions. Characteristic Raman bands for calcite are at 281, 712, and 1086 cm^{-1}.

In addition, three calcium-binding proteins are found in the shell of *P. placenta*, including EFCB6, hemicentin-1 and EGFL6 (Table 1), which were found in a few different mollusk shells.[68,69,98–101] EFCB6 plays an important role in calcium metabolism during shell formation by regulating calcium uptake, transport, and secretion.[98] EGFL6 was first identified from *C. gigas*,[100] while EGF-like domains are associated with biological functions such as cell adhesion, signaling, and Ca^{2+} binding.[68] Hemicentin-1 is found in the coral skeletal

organic matrix and usually possesses Ca^{2+}-binding function in *Lingula*.[69,99] Elongation factor 1-alpha (EF1-α) was highly expressed in the mantle tissue compared to other tissues in the pearl oyster *Pinctada martensii*, which was proposed to have a potential function for biomineralization.[102]

Amino acid analysis indicates that three primary amino acid residues include aspartic acid (Asp), serine (Ser) and glycine (Gly) for the ASM from shells of *P. placenta* (Table 1), which altogether occupy 44.54 mol%, while there are 64.44 mol% in total for the detected amino acids. Both Ser and Asp contain carboxylic groups and were reported to inhibit nucleation of $CaCO_3$.[84] Furthermore, it is reported that proteins with carboxylic groups[22,103] or Asprich groups[104] extracted from mollusk shells can stabilize ACC. Ca^{2+} can be concentrated by proteins with carboxylic groups or calcium-binding proteins.[67] Thus, we propose that the Asp and Ser groups of the ASM may play a primary role in complexation with Ca^{2+} and stabilization of ACC. Indeed, complexation of Ca^{2+} and ASM can be observed by TEM, EDS and Tyndall effect before the addition of CO_2 to the reaction solution. The ASM was also found to stabilize ACC and inhibit nucleation according to the titration, TEM, SAED and FTIR results in this work. Interestingly, acidic biomolecules were also reported to stabilize amorphous calcium phosphate (ACP). Albumin and acidic proteins can inhibit calcium phosphate precipitation and stabilize the amorphous phase.[105] The biomolecule casein phosphopeptide also has a strong influence on the stabilization of ACP.[106,107] Calcium ions are bound to the polymers by complexation through acidic groups such as PAA, poly-Asp and poly-Glu can stabilize amorphous calcium phosphate and inhibit the hydroxyapatite nucleation from ACP and crystallization process.[108]

A schematic diagram was drawn to show the formation process of *in vitro* crystallization of $CaCO_3$ on the shell surface of *P. placenta* in Fig. 11. There are few stages for the *in vitro* crystallization process. In stage I, a complex of Ca^{2+} and ASM form in the solution. In stage II, ACC nanoparticles with a size of about 30–50 nm form in the solution after 20 min of gas diffusion process, which were transformed *via* the complex of Ca^{2+} and the ASM. The reaction system proceeds as stage II from 20 min to 10 h of reaction. In stage III, calcite nanoparticles of about 50 nm nucleate on the edges of the calcite laths of *P. placenta via* secondary nucleation. Stage IV is the epitaxial growth of calcite crystals on the surface of the calcite laths of *P. placenta*, which is a very fast process; it takes about 50 min for the calcite nanocrystals to grow from 50 nm to 10 μm.

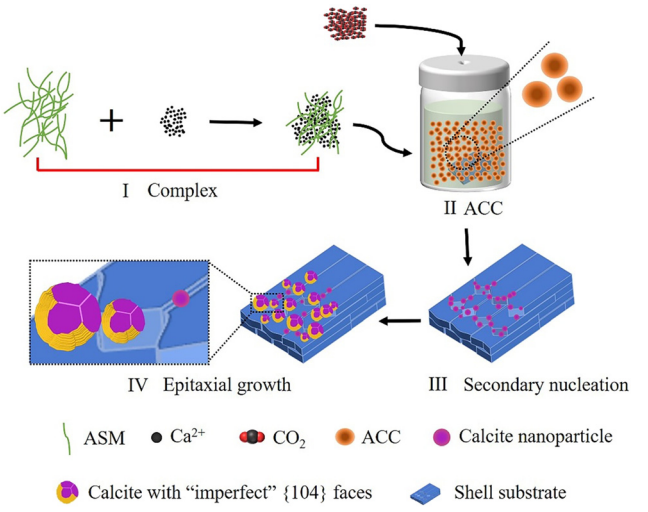

Fig. 11 A schematic diagram for the formation process of *in vitro* crystallization of $CaCO_3$ on the shell surface of *P. placenta*.

The influence of ASM extracted from aragonite or calcite biominerals such as nacre or prisms of mollusk shells on the *in vitro* crystallization of calcium carbonate has been investigated by many research groups. Biological molecules can influence the morphology of calcite by adsorbing onto the kink sites, step edges, or particular faces[109] of calcite. There might be preferred adsorption or non-specific adsorption on some crystalline directions, steps or faces of calcite. Except for adsorption on particular faces or directions, biological molecules may also be occluded in the crystals and influence the crystallization process.[110] As far as we know, this is the first report on the influence of ASM extracted from foliated calcite laths of mollusk shells on the *in vitro* crystallization. According to the experimental results, the ASM extracted from *P. placenta* has a strong effect on the stabilization of ACC and inhibition of nucleation. The ASM can inhibit the (secondary) nucleation of calcite and stabilize ACC for 10 h and 24 h on the glass substrate and the surface of foliated calcite laths of *P. placenta*, respectively. *In vitro* crystallization of the calcite system shows that ASM has a strong influence on the morphology of calcite, and more rounded calcite microcrystals form and partial {104} faces disappear while increasing the concentration of ASM. Spherical or rounded calcite crystals were formed in the presence of additives.[4–7,111] Kim *et al.* showed that aspartic acid (Asp) and glycine can be incorporated into calcite single crystals, induce the formation of sphere-like calcite crystals and strongly increase the hardness of calcite,[4] while micelles can also be occluded and enhance the mechanical properties of calcite.[5,6] These spherical calcite crystals can also be formed in the presence of gelatine.[7] It is clear that the obtained rounded calcite microcrystals are very different from the foliated calcite crystals of the shells of *P. placenta*. A possible reason is that the ASM does not contain the proteins which have a key function for the formation of foliated shapes of calcite. Poly(acrylic acid) (PAA), poly(allylamine hydrochloride) (pAH) and poly-L-aspartic acid (pAsp) can inhibit the nucleation and growth of calcium carbonate.[112–114] Pif97 from the nacreous layer of *P. fucata* with acidic amino acid residues can stabilize ACC and inhibit calcite growth.[47]

Generally, Ca^{2+}-binding and framework-associated proteins were identified in the ASM of the foliated calcite layer of *P. placenta*, which show a strong effect on the stabilization of ACC and inhibition of nucleation and

influence the final morphology of calcite by adsorption on the surface of some step edges or faces and occlusion into calcite crystals. It would be important to extract these proteins and investigate their individual functions for biomineralization *via in vitro* crystallization of $CaCO_3$ in the future.

5 Conclusions

In this work, sixteen proteins were identified in the ASM extracted from the shells of *P. placenta* by proteomics analysis. Proteomics analysis shows that there are four framework-associated proteins, three Ca^{2+}-binding proteins, and one potentially mineralization-related protein, which are supposed to be related to the biomineralization process. In addition, the ASM was enriched in Gly, Asp and Ser, which might contribute to complexation of the ASM and Ca^{2+} and stabilization of ACC in the *in vitro* crystallization system. We found that the ASM can stabilize ACC and inhibit the secondary nucleation of calcium carbonate for 10 h on the shell surface of *P. placenta* in aqueous solution. An explosive secondary nucleation and quick crystal growth from 50 nm to 10 μm can be finished on the shell surface in one hour, in between 10 h and 11 h of reaction time, *via* a gas diffusion process. Meanwhile, the addition of ASM affects the final morphology of calcite crystals and leads to the formation of rounded calcite crystals with "imperfect" {104} faces. The calcite crystals formed on the shell surfaces become more and more rounded and lose {104} planes with the increase of the concentrations of ASM in the solution. CLSM analysis revealed that the ASM does not adsorb on the crystal surfaces but actually occludes into the calcite crystals. The above results might shed light on the functional study of ASM during biomineralization.

Data availability

All relevant data reported here are included in the main section of the manuscript or in the ESI.† All described materials are available upon request.

Author contributions

Ningjing Song performed the main experiments, data analysis, and wrote the paper. Yurong Ma designed the experiments and revised the manuscript. All authors read and approved the final manuscript.

Conflicts of interest

There are no conflicts to declare.

Acknowledgements

This research was funded by the National Natural Science Foundation of China (Grant No. 21877009) and the Beijing Institute of Technology Research Fund Program for Young Scholars. This work was also supported by the facilities at the Analysis & Testing Center, Beijing Institute of Technology.

References

1 L. Addadi, D. Joester, F. Nudelman and S. Weiner, *Chem. – Eur. J.*, 2006, **12**, 980–987.
2 L. B. Gower, *Chem. Rev.*, 2008, **108**, 4551–4627.
3 F. Marin, G. Luquet, B. Marie and D. Medakovic, *Curr. Top. Dev. Biol.*, 2008, **80**, 209–276.
4 Y. Y. Kim, J. D. Carloni, B. Demarchi, D. Sparks, D. G. Reid, M. E. Kunitake, C. C. Tang, M. J. Duer, C. L. Freeman, B. Pokroy, K. Penkman, J. H. Harding, L. A. Estroff, S. P. Baker and F. C. Meldrum, *Nat. Mater.*, 2016, **15**, 903–910.
5 K. R. Cho, Y.-Y. Kim, P. Yang, W. Cai, H. Pan, A. N. Kulak, J. L. Lau, P. Kulshreshtha, S. P. Armes, F. C. Meldrum and J. J. De Yoreo, *Nat. Commun.*, 2016, **7**, 10187.
6 Y.-Y. Kim, K. Ganesan, P. Yang, A. N. Kulak, S. Borukhin, S. Pechook, L. Ribeiro, R. Kroeger, S. J. Eichhorn, S. P. Armes, B. Pokroy and F. C. Meldrum, *Nat. Mater.*, 2011, **10**, 890–896.
7 Y. X. Huang, J. Buder, R. Cardoso-Gil, Y. Prots, W. Carrillo-Cabrera, P. Simon and R. Kniep, *Angew. Chem., Int. Ed.*, 2008, **47**, 8280–8284.
8 D. Gebauer, A. Volkel and H. Colfen, *Science*, 2008, **322**, 1819–1822.
9 E. M. Pouget, P. H. H. Bomans, J. A. C. M. Goos, P. M. Frederik, G. de With and N. A. J. M. Sommerdijk, *Science*, 2009, **323**, 1455–1458.
10 Z. Zou, J. E. M. Habraken Wouter, G. Matveeva, C. S. Jensen Anders, L. Bertinetti, A. Hood Matthew, C.-y. Sun, U. P. A. Gilbert Pupa, I. Polishchuk, B. Pokroy, J. Mahamid, Y. Politi, S. Weiner, P. Werner, S. Bette, R. Dinnebier, U. Kolb, E. Zolotoyabko and P. Fratzl, *Science*, 2019, **363**, 396–400.
11 Z. Liu, C. Shao, B. Jin, Z. Zhang, Y. Zhao, X. Xu and R. Tang, *Nature*, 2019, **574**, 394–398.
12 F. Marin, N. Le Roy and B. Marie, *Front. Biosci.*, 2012, **4**, 125.
13 A. G. Checa, E. M. Harper and A. González-Segura, *Sci. Rep.*, 2018, **8**, 7507.
14 F. J. Esteban-Delgado, E. M. Harper, A. G. Checa and A. B. Rodríguez-Navarro, *Biol. Bull.*, 2008, **214**, 153–165.
15 A. G. Checa, *Front. Mar. Sci.*, 2018, **5**, 353.
16 B. J. A. Runnegar, *Alcheringa*, 1984, **8**, 273–290.
17 A. G. Checa, F. J. Esteban-Delgado and A. B. Rodríguez-Navarro, *J. Struct. Biol.*, 2007, **157**, 393–402.
18 L. Li and C. Ortiz, *Adv. Mater.*, 2013, **25**, 2344–2350.
19 L. Li and C. Ortiz, *Nat. Mater.*, 2014, **13**, 501–507.
20 N. Song, J. Li, B. Li, E. Pan and Y. Ma, *Sci. Rep.*, 2022, **12**, 4743.
21 C. Pan, D. Fang, G. Xu, J. Liang, G. Zhang, H. Wang, L. Xie and R. Zhang, *J. Biol. Chem.*, 2013, **289**, 2776–2787.
22 L. Addadi, S. Raz and S. Weiner, *Adv. Mater.*, 2003, **15**, 959–970.
23 D. Gebauer, *Minerals*, 2018, **8**, 179.
24 Y. Xu, K. C. H. Tijssen, P. H. H. Bomans, A. Akiva, H. Friedrich, A. P. M. Kentgens and N. A. J. M. Sommerdijk, *Nat. Commun.*, 2018, **9**, 2582.

25 P. J. M. Smeets, A. R. Finney, W. J. E. M. Habraken, F. Nudelman, H. Friedrich, J. Laven, J. J. De Yoreo, P. M. Rodger and N. A. J. M. Sommerdijk, *Proc. Natl. Acad. Sci. U. S. A.*, 2017, **114**, E7882–E7890.
26 D. Gebauer, P. Raiteri, J. D. Gale and H. Cölfen, *Am. J. Sci.*, 2018, **318**, 969–988.
27 M. Kellermeier, A. Picker, A. Kempter, H. Cölfen and D. Gebauer, *Adv. Mater.*, 2014, **26**, 752–757.
28 M. Farhadi-Khouzani, D. M. Chevrier, P. Zhang, N. Hedin and D. Gebauer, *Angew. Chem., Int. Ed.*, 2016, **55**, 8117–8120.
29 C. Rodriguez-Navarro, K. Kudłacz, Ö. Cizer and E. Ruiz-Agudo, *CrystEngComm*, 2015, **17**, 58–72.
30 P. J. M. Smeets, K. R. Cho, R. G. E. Kempen, N. A. J. M. Sommerdijk and J. J. De Yoreo, *Nat. Mater.*, 2015, **14**, 394–399.
31 A. Dey and N. A. J. M. Sommerdijk, *Chem. Soc. Rev.*, 2010, **39**, 397–409.
32 M. H. Nielsen, S. Aloni and J. J. De Yoreo, *Science*, 2014, **345**, 1158–1162.
33 A. Dey, P. H. Bomans, F. A. Müller, J. Will, P. M. Frederik, G. de With and N. A. Sommerdijk, *Nat. Mater.*, 2010, **9**, 1010–1014.
34 R. Demichelis, P. Raiteri, J. D. Gale, D. Quigley and D. Gebauer, *Nat. Commun.*, 2011, **2**, 590.
35 D. Gebauer and H. Cölfen, *Nano Today*, 2011, **6**, 564–584.
36 D. Gebauer, M. Kellermeier, J. D. Gale, L. Bergstrom and H. Coelfen, *Chem. Soc. Rev.*, 2014, **43**, 2348–2371.
37 P. J. Smeets, K. R. Cho, R. G. Kempen, N. A. Sommerdijk and J. J. De Yoreo, *Nat. Mater.*, 2015, **14**, 394–399.
38 Z. Liu, Z. Zhang, Z. Wang, B. Jin, D. Li, J. Tao, R. Tang and J. J. De Yoreo, *Proc. Natl. Acad. Sci. U. S. A.*, 2020, **117**, 3397–3404.
39 J. D. Rimer, *Proc. Natl. Acad. Sci. U. S. A.*, 2020, **117**, 3360–3362.
40 H. Du, M. Steinacher, C. Borca, T. Huthwelker, A. Murello, F. Stellacci and E. Amstad, *J. Am. Chem. Soc.*, 2018, **140**, 14289–14299.
41 A. V. Radha, T. Z. Forbes, C. E. Killian, P. U. P. A. Gilbert and A. Navrotsky, *Proc. Natl. Acad. Sci. U. S. A.*, 2010, **107**, 16438–16443.
42 F. Sebastiani, S. L. P. Wolf, B. Born, T. Q. Luong, H. Cölfen, D. Gebauer and M. Havenith, *Angew. Chem., Int. Ed.*, 2017, **56**, 490–495.
43 A. Gal, W. Habraken, D. Gur, P. Fratzl, S. Weiner and L. Addadi, *Angew. Chem., Int. Ed.*, 2013, **52**, 4867–4870.
44 G. Falini, S. Albeck, S. Weiner and L. Addadi, *Science*, 1996, **271**, 67–69.
45 J. Kong, C. Liu, D. Yang, Y. Yan, Y. Chen, Y. Liu, G. Zheng, L. Xie and R. Zhang, *CrystEngComm*, 2019, **21**, 1250–1261.
46 Y. Politi, J. Mahamid, H. Goldberg, S. Weiner and L. Addadi, *CrystEngComm*, 2007, **9**, 1171–1177.
47 S. Y. Bahn, B. H. Jo, B. H. Hwang, Y. S. Choi and H. J. Cha, *Cryst. Growth Des.*, 2015, **15**, 3666–3673.
48 L. Treccani, K. Mann, F. Heinemann and M. Fritz, *Biophys. J.*, 2006, **91**, 2601–2608.
49 Y. Yan, D. Yang, X. Yang, C. Liu, J. Xie, G. Zheng, L. Xie and R. Zhang, *Sci. Rep.*, 2017, **7**, 6021.
50 J. Kong, C. Liu, D. Yang, Y. Yan, Y. Chen, J. Huang, Y. Liu, G. Zheng, L. Xie and R. Zhang, *Cryst. Growth Des.*, 2018, **18**, 3794–3804.
51 J. Liang, G. Xu, J. Xie, I. Lee, L. Xiang, H. Wang, G. Zhang, L. Xie and R. Zhang, *PLoS One*, 2015, **10**, e0131868.
52 M. Suzuki, E. Murayama, H. Inoue, N. Ozaki, H. Tohse, T. Kogure and H. Nagasawa, *Biochem. J.*, 2004, **382**, 205–213.
53 T. Takeuchi, I. Sarashina, M. Iijima and K. Endo, *FEBS Lett.*, 2008, **582**, 591–596.
54 G. Fu, S. Valiyaveettil, B. Wopenka and D. E. Morse, *Biomacromolecules*, 2005, **6**, 1289–1298.
55 X. Wang, C. Wu, K. Tao, K. Zhao, J. Wang, H. Xu, D. Xia, H. Shan and J. R. Lu, *J. Phys. Chem. B*, 2010, **114**, 5301–5308.
56 M. Różycka, M. Wojtas, M. Jakób, C. Stigloher, M. Grzeszkowiak, M. Mazur and A. Ożyhar, *PLoS One*, 2014, **9**, e114308.
57 J. B. Thompson, G. T. Paloczi, J. H. Kindt, M. Michenfelder, B. L. Smith, G. Stucky, D. E. Morse and P. K. Hansma, *Biophys. J.*, 2000, **79**, 3307–3312.
58 D. Fang, C. Pan, H. Lin, Y. Lin, G. Xu, G. Zhang, H. Wang, L. Xie and R. Zhang, *PLoS One*, 2012, **7**, e35715.
59 X. Bourrat, L. Qiao, Q. Feng, M. Angellier, A. Dissaux, J.-M. Beny, V. Barbin, P. Stempflé, M. Rousseau and E. Lopez, *Mater. Charact.*, 2012, **72**, 94–103.
60 Y. Ma, L. Qiao and Q. Feng, *Mater. Sci. Eng., C*, 2012, **32**, 1963–1970.
61 K. Gries, F. Heinemann, M. Gummich, A. Ziegler, A. Rosenauer and M. Fritz, *Cryst. Growth Des.*, 2011, **11**, 729–734.
62 B. Marie, C. Joubert, A. Tayale, I. Zanella-Cléon, C. Belliard, D. Piquemal, N. Cochennec, F. Marin, Y. Gueguen and C. Montagnani, *Proc. Natl. Acad. Sci. U. S. A.*, 2012, **109**, 20986–20991.
63 K. Mann, N. Cerveau, M. Gummich, M. Fritz, M. Mann and D. Jackson, *Proteome Sci.*, 2018, **16**, 11.
64 B. Marie, A. Marie, D. Jackson, L. Dubost, B. Degnan, C. Milet and F. Marin, *Proteome Sci.*, 2010, **8**, 54.
65 J. M. Manns, *Curr. Protoc. Microbiol.*, 2011, **22**, A.3M.1–A.3M.13.
66 J. Aizenberg, J. Hanson, T. Koetzle, S. Weiner and L. Addadi, *J. Am. Chem. Soc.*, 1997, **119**, 881–886.
67 J. Huang, C. Zhang, Z. Ma, L. Xie and R. Zhang, *Biochim. Biophys. Acta*, 2007, **1770**, 1037–1044.
68 P. Maurer and E. Hohenester, *Matrix Biol.*, 1997, **15**, 569–580.
69 Y.-J. Luo, T. Takeuchi, R. Koyanagi, L. Yamada, M. Kanda, M. Khalturina, M. Fujie, S.-i. Yamasaki, K. Endo and N. Satoh, *Nat. Commun.*, 2015, **6**, 8301.
70 I. M. Weiss, V. Schönitzer, N. Eichner and M. Sumper, *FEBS Lett.*, 2006, **580**, 1846–1852.
71 C. Jin, J. Zhao, J. Pu, X. Liu and J. Li, *Int. J. Biol. Macromol.*, 2019, **135**, 745–751.
72 W. Müller, A. Borejko, D. Brandt, R. Osinga, H. Ushijima, B. Hamer, A. Krasko, X. Cao, I. Müller and H. C. Schröder, *FEBS J.*, 2005, **272**, 3838–3852.

73 H. Miyamoto, F. Miyoshi and J. Kohno, *Zool. Sci.*, 2005, **22**, 311–315.
74 C. A. Whittaker and R. O. Hynes, *Mol. Biol. Cell*, 2002, **13**, 3369–3387.
75 Y. Shi, C. Yu, Z. Gu, X. Zhan, Y. Wang and A. Wang, *Mar. Biotechnol.*, 2013, **15**, 175–187.
76 M. Gerdol, C. Manfrin, G. De Moro, A. Figueras, B. Novoa, P. Venier and A. Pallavicini, *Dev. Comp. Immunol.*, 2011, **35**, 635–643.
77 C. Liu and R. Zhang, *J. Proteomics*, 2021, **238**, 104171.
78 X.-J. Hu, T. Li, Y. Wang, Y. Xiong, X.-H. Wu, D.-L. Zhang, Z.-Q. Ye and Y.-D. Wu, *Sci. Rep.*, 2017, **7**, 10585–10585.
79 M. Kellermeier, H. Cölfen and D. Gebauer, *Methods Enzymol.*, 2013, **532**, 45–69.
80 I. Perovic, E. P. Chang, M. Lui, A. Rao, H. Cölfen and J. S. Evans, *Biochemistry*, 2014, **53**, 2739–2748.
81 I. Perovic, A. Verch, E. P. Chang, A. Rao, H. Cölfen, R. Kröger and J. S. Evans, *Biochemistry*, 2014, **53**, 7259–7268.
82 A. Verch, D. Gebauer, M. Antonietti and H. Colfen, *Phys. Chem. Chem. Phys.*, 2011, **13**, 16811–16820.
83 M. Pendola, G. Jain, Y. C. Huang, D. Gebauer and J. S. Evans, *ACS Omega*, 2018, **3**, 11823–11830.
84 A. Picker, M. Kellermeier, J. Seto, D. Gebauer and H. Colfen, *Z. Kristallogr. - Cryst. Mater.*, 2012, **227**, 744–757.
85 D. Gebauer, H. Colfen, A. Verch and M. Antonietti, *Adv. Mater.*, 2009, **21**, 435–439.
86 A. Rao, J. K. Berg, M. Kellermeier and D. Gebauer, *Eur. J. Mineral.*, 2014, **26**, 537–552.
87 A. Rao, J. Seto, J. K. Berg, S. G. Kreft, M. Scheffner and H. Colfen, *J. Struct. Biol.*, 2013, **183**, 205–215.
88 Y. Zhang, L. Qiao, H. Yan, I. Zizak, P. Zaslansky, Y. Li, L. Qi and Y. Ma, *Cryst. Growth Des.*, 2020, **20**, 3482–3492.
89 D. Yang, Y. Yan, X. Yang, J. Liu, G. Zheng, L. Xie and R. Zhang, *J. Biol. Chem.*, 2019, **294**, 8371–8383.
90 Y.-Y. Kim, C. L. Freeman, X. Gong, M. A. Levenstein, Y. Wang, A. Kulak, C. Anduix-Canto, P. A. Lee, S. Li, L. Chen, H. K. Christenson and F. C. Meldrum, *Angew. Chem., Int. Ed.*, 2017, **56**, 11885–11890.
91 C. Jin, J.-L. Li and X.-J. Liu, *Int. J. Biol. Macromol.*, 2020, **150**, 1229–1237.
92 M. Różycka, I. Coronado, K. Brach, J. Olesiak-Bańska, M. Samoć, M. Zarębski, J. Dobrucki, M. Ptak, E. Weber and I. Polishchuk, *Chemistry*, 2019, **25**, 12740–12750.
93 A. Gal, K. Kahil, N. Vidavsky, R. T. DeVol, P. U. P. A. Gilbert, P. Fratzl, S. Weiner and L. Addadi, *Adv. Funct. Mater.*, 2014, **24**, 5420–5426.
94 P. Gao, Z. Liaozhi, X.-X. Wang, L.-F. Bao, M.-H. Fan, X.-M. Li, C.-W. Wu and S.-W. Xia, *PLoS One*, 2015, **10**, e0133913.
95 Z. Liaozhi, L.-F. Bao, M.-H. Fan, P. Gao, X.-X. Wang, C.-L. Qin and X.-M. Li, *J. Proteomics*, 2015, **122**, 26–40.
96 X. Liu, S. Zeng, S. Dong, C. Jin and L. J. Jiale, *PLoS One*, 2015, **10**, e0135123.
97 X. Du, G. Fan, Y. Jiao, H. Zhang, X. Guo, R. Huang, Z. Zheng, C. Bian, Y. Deng, Z.-D. Wang, X. Liang, H. Liang, C. Shi, X. Zhao, F. Sun, R. Hao, J. Bai, J. Liu and X. Liu, *GigaScience*, 2017, **6**, 1–12.
98 H. Miyamoto, T. Miyashita, M. Okushima, S. Nakano, T. Morita and A. Matsushiro, *Proc. Natl. Acad. Sci. U. S. A.*, 1996, **93**, 9657–9660.
99 P. Ramos-Silva, J. Kaandorp, L. Huisman, B. Marie, I. Zanella-Cléon, N. Guichard, D. J. Miller and F. Marin, *Mol. Biol. Evol.*, 2013, **30**, 2099–2112.
100 B. Marie, I. Zanella-Cléon, N. Guichard, M. Becchi and F. Marin, *Mar. Biotechnol.*, 2011, **13**, 1159–1168.
101 G. Zhang, X. Fang, X. Guo, L. I. Li, R. Luo, F. Xu, P. Yang, L. Zhang, X. Wang and H. Qi, *Nature*, 2012, **490**, 49–54.
102 Y. Shi, C. Yu, Z. Gu, X. Zhan, Y. Wang and A. Wang, *Mar. Biotechnol.*, 2012, **15**, 175–187.
103 J. Aizenberg, L. Addadi, S. Weiner and G. Lambert, *Adv. Mater.*, 1996, **8**, 222–226.
104 B. A. Gotliv, N. Kessler, J. L. Sumerel, D. E. Morse, N. Tuross, L. Addadi and S. Weiner, *ChemBioChem*, 2005, **6**, 304–314.
105 A. Heiss, T. Eckert, A. Aretz, W. Richtering, W. van Dorp, C. Schäfer and W. Jahnen-Dechent, *J. Biol. Chem.*, 2008, **283**, 14815–14825.
106 K. J. Cross, N. L. Huq and E. C. Reynolds, *Biochemistry*, 2016, **55**, 4316–4325.
107 P. De Sa Peixoto, J. V. Silva, G. Laurent, M. Schmutz, D. Thomas, A. Bouchoux and G. Gésan-Guiziou, *Langmuir*, 2017, **33**, 1256–1264.
108 S. Jiang, H. Pan, Y. Chen, X. Xu and R. Tang, *Faraday Discuss.*, 2015, **179**, 451–461.
109 E. Weber and B. Pokroy, *CrystEngComm*, 2015, **17**, 5873–5883.
110 M. Fu, A. Wang, X. Zhang, L. Dai and J. Li, *Angew. Chem., Int. Ed.*, 2016, **55**, 908–911.
111 W. Song, S. Y. Bahn, H. J. Cha, S. P. Pack and Y. S. Choi, *Biotechnol. Lett.*, 2016, **38**, 809–816.
112 K. Naka, S.-C. Huang and Y. Chujo, *Langmuir*, 2006, **22**, 7760–7767.
113 M. Sancho-Tomás, S. Fermani, M. A. Durán-Olivencia, F. Otálora, J. Gómez-Morales, G. Falini and J. M. García-Ruiz, *Cryst. Growth Des.*, 2013, **13**, 3884–3891.
114 B. Cantaert, Y.-Y. Kim, H. Ludwig, F. Nudelman, N. A. J. M. Sommerdijk and F. C. Meldrum, *Adv. Funct. Mater.*, 2012, **22**, 907–915.